Supplementary Information

Recognition, classification and prediction of tactile sense

Sungwoo Chun, Inyoung Hwang, Wonkyeong Son, Joon-Hyuk Chang and Wanjun Park*

Department of Electronics and Computer Engineering, Hanyang University, Seoul 04763 South Korea

S1. Tactile-sensor fabrication

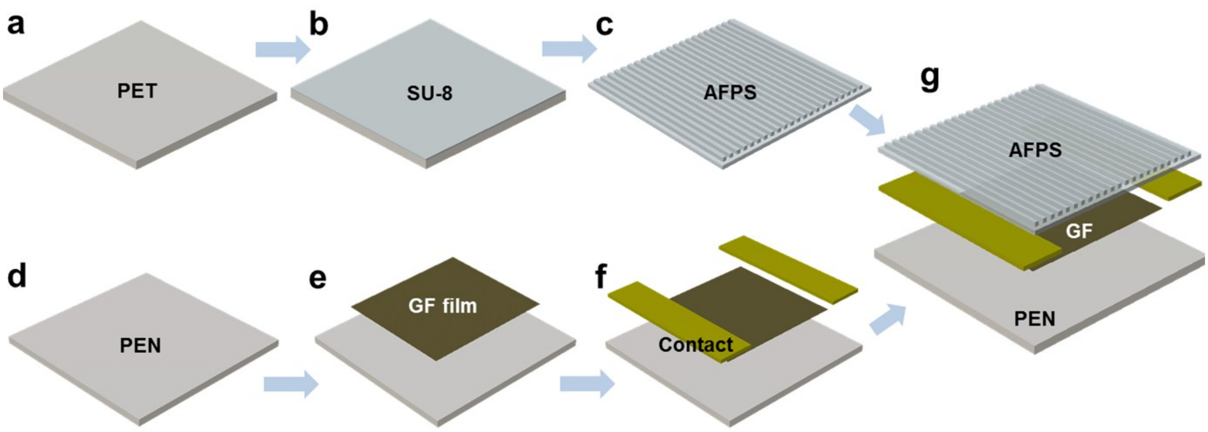

Figure S1-1. Process steps for tactile-sensor fabrication. (a) PET substrate. (b) Coating of SU-8 photoresist. (c) Optical lithography for an AFPS which is ridge patterns with a line width, height, and separation of 300, 70, and 600 µm, respectively. (d) PEN substrate. (e) Spray coating of the GF film. (f) Formation of Pt electrodes. (g) Tactile sensor device with assembly.

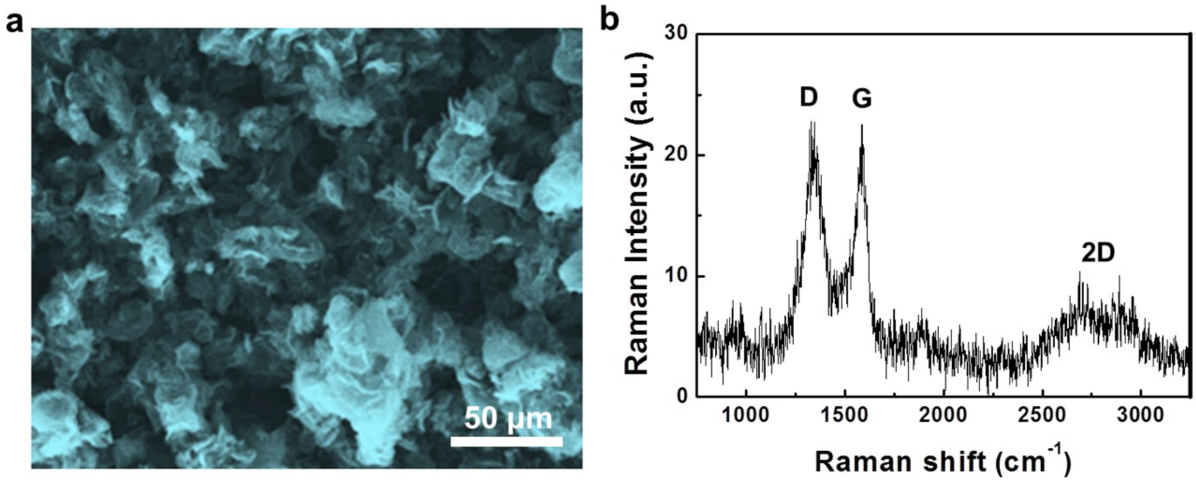

Figure S1-2. Graphene film characteristics. (a) Scanning electron microscopy (SEM) image of the GF film with a naturally formed porous structure. Numerous spaces are used as direct pressure absorbers inducing piezo-resistive characters that are attributed to the main operating principle of the tactile sensor. (b) Raman spectrum for the GF film. The excitation wavelength is 514 nm and the laser power is 2 mW. The Raman resonances of the film indicate that the GF film is multi-layered graphenes, including many defects.

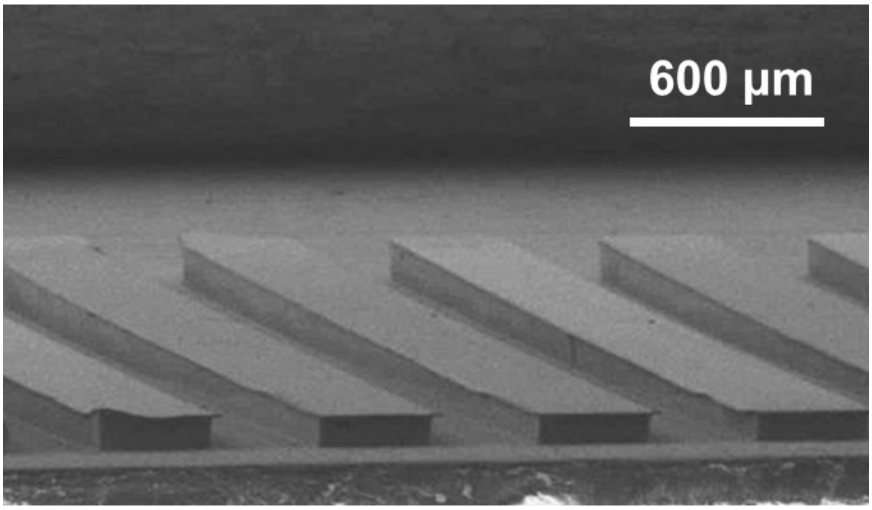

Figure S1-3. Scanning electron microscopy (SEM) image of the AFPS applied to the tactile sensor.

S2. Basic sensor characteristics of the graphene force sensor

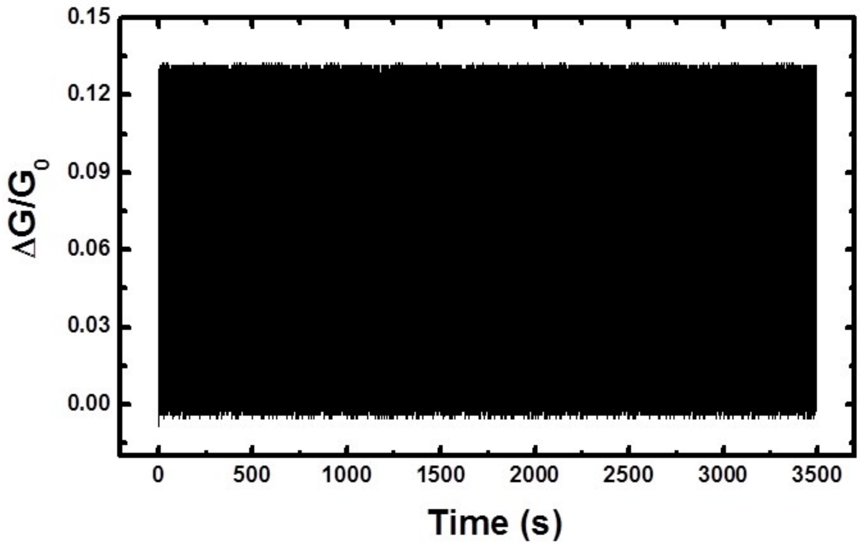

Figure S2-1. Reproducible operation of the force sensor. The sensor shows the consistent responses during 10,000 loading-unloading cycles with 50 kPa of the applied pressure whose pulse width is 3 Hz of frequency and measurement interval is 1 ms.

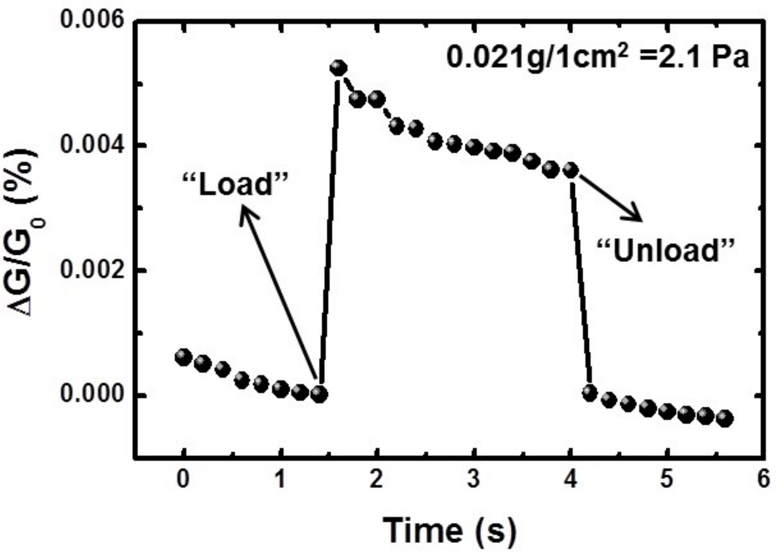

Figure S2-2. Minimum detecting pressure of the force sensor. The sensor is detectable for the vertical pressure as low as 2.1 Pa driven by a weight of 21 mg on 1 cm^2 contact area.

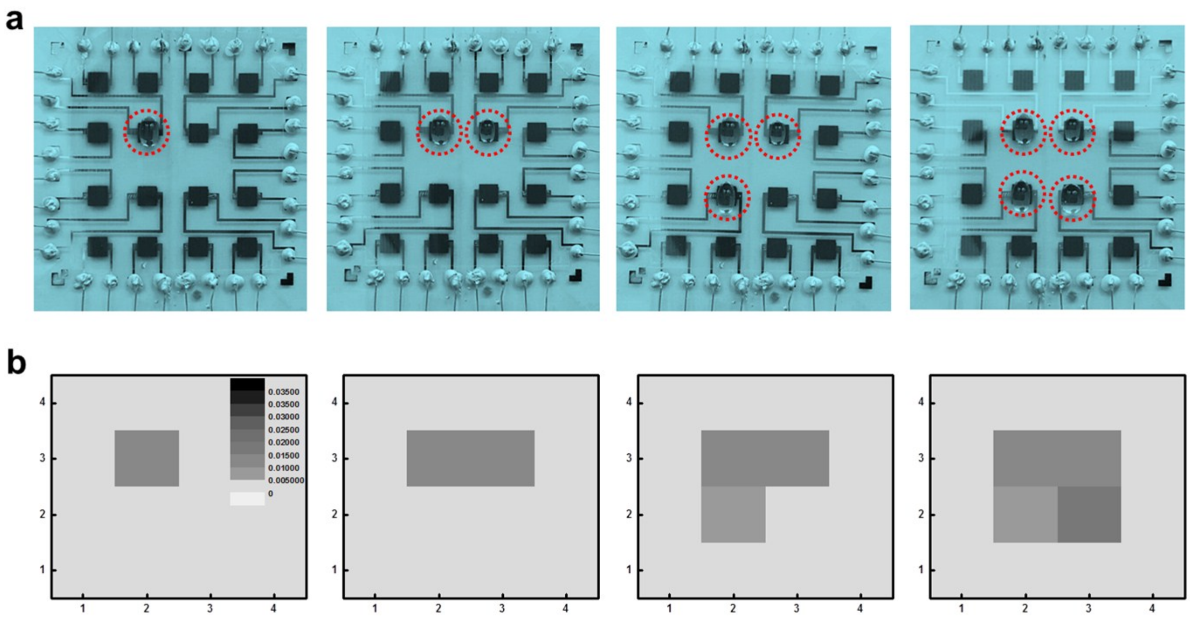

Figure S2-3. Force sensor array characteristic. (a) Photographs of a 4×4 sensor array with water droplet inducing ~52 Pa. (b) Conductance change mappings of pressure distributions for the droplets.

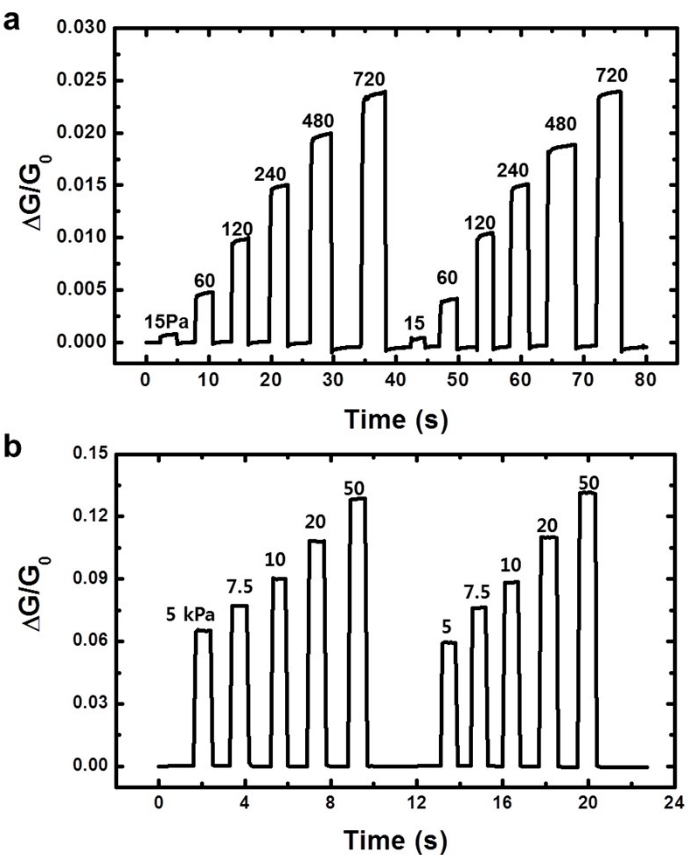

Figure S2-4. Sensing capability of the sensor for (a) low pressure region of 15–720 Pa and (b) high pressure region of 5– 50 kPa.

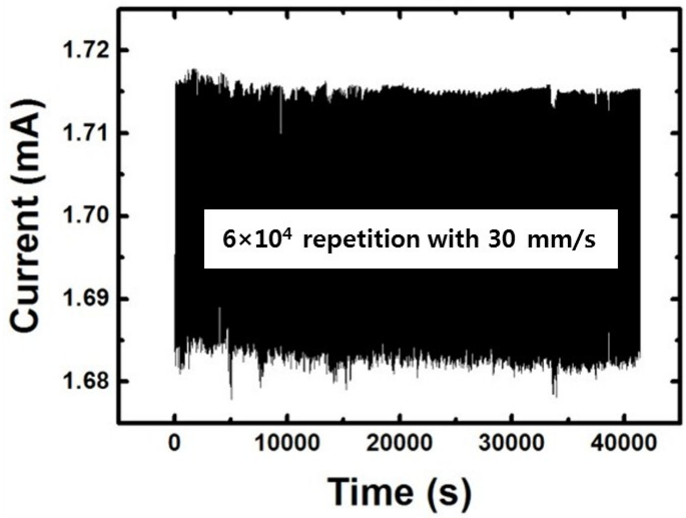

Figure S2-5. Reproducible operation for rubbing on the tactile sensor. The sensor shows the consistent responses during 60,000 cycles of repetitions for touching and rubbing on a smooth surface for rubbing distance of 1cm with velocity of ~ 30 mm/s.

S3. Frequency response characteristic depending on periodic distance of patterned ridge

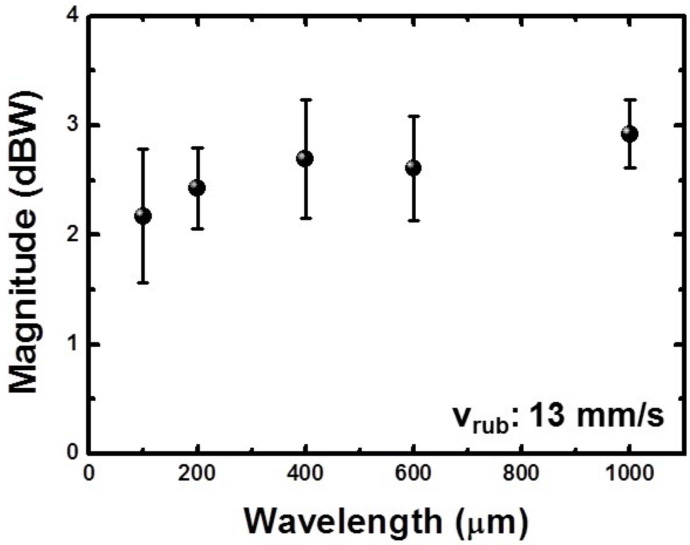

Figure S3. SNR in power spectrum. The sensor maintains the signal-to-noise ratio (SNR) above 2 dB in power spectrum down to 100 μm of periodic distance of the ridge patterns in the AFTS. The rubbing velocity was 13 mm/s for this measurement.

S4. Pre-processing method for noise removal and normalization

The electric signal collected from the tactile sensor output is expressed as follows [1]:

$$y(t) = x(t) + n(t) + b(t) \qquad (1)$$

where $x(t)$, $n(t)$, and $b(t)$ denote tactile signal, noise signal, and bias signal, respectively. With the general characteristics of noise due to rapid fluctuation, the de-noised tactile signal is obtained by the moving-average method with short context window as follows:

$$\hat{y}(t) = \frac{1}{2N+1}\sum_{j=-N}^{N} y(j) \approx y(t) - n(t) = x(t) + b(t) \qquad (2)$$

where N denotes the length of the window for noise removal. On the other hand, the bias signal described by low-frequency component is estimated by applying the moving-average method with long context window in time domain as follows:

$$b(t) \approx \frac{1}{2M+1}\sum_{j=-M}^{M} y(j) \qquad (3)$$

where M denotes length of the window for bias signal estimation. Then the tactile signal becomes:

$$x(t) = \hat{y}(t) - b(t). \qquad (4)$$

The normalization process is additionally performed to correct the tactile signal containing variances due to inconsistency in rubbing speed and vertical pressure during touching measurement. For this correction, the autocorrelation is driven to estimate the period of the tactile signal as follows:

$$r(\tau) = \frac{1}{K}\sum_{j=1}^{K-1} \hat{y}_n(j)\hat{y}_n(j-\tau) \qquad (5)$$

where K denotes the length of context and n denotes the frame index. It is noted that there are

1648 frames per each testing sample for this work. Then, the period of the tactile signal at n-th frame is obtained as the index τ corresponding to the maximum value as follows:

$$p(n) = argmax_{\tau} r(\tau) \quad (6)$$

If the period is longer than the target value, the high-frequency components are removed by the finite impulse response (FIR) low pass filter (LPF), and then the period of the tactile signal is regularized via an interpolation in time domain. If not, resampling process is performed. With proportionality between the peak-to-peak of bias signal in the sensor output and the applied pressure on the sensor, the amplitude of interaction is regularized by

$$\hat{x}(n) = x(n)/peak - to - peak(n) \quad (7)$$

with

$$peak - to - peak(n) = \max(b(n)) - \min(b(n)) \quad (8)$$

As a result, the pure tactile signal, $\hat{x}(n)$, is finally constructed for the feature extraction process.

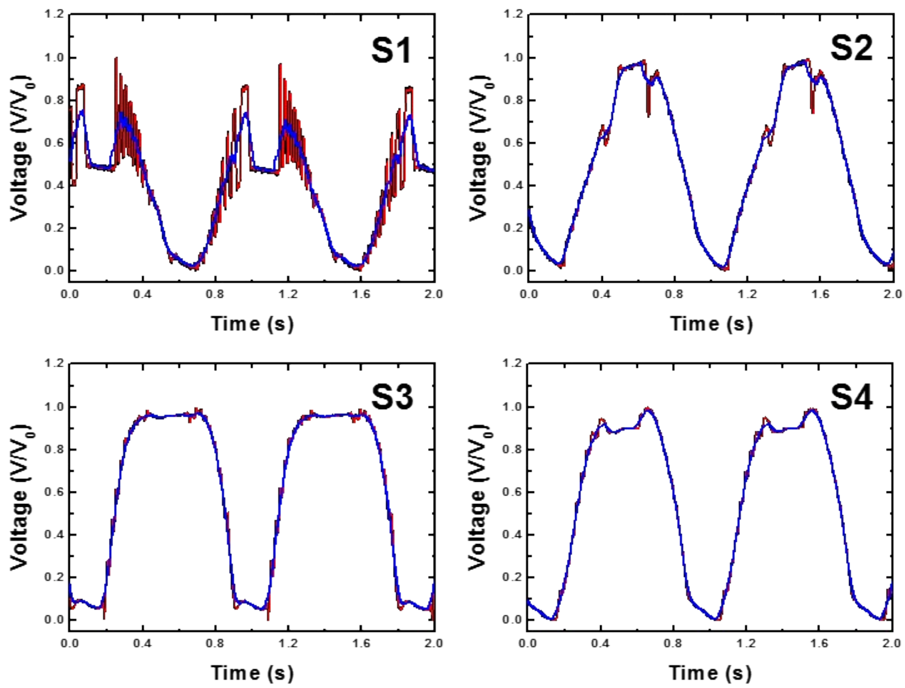

Figure S4-1. Noise removal processes from the senor signals. For the 4 different tactile pattern samples described in chapter 2.3, the de-noised tatile signal (x(t), red), and the bias signal (b(t), blue) are described on the sensor outpup signal (black).

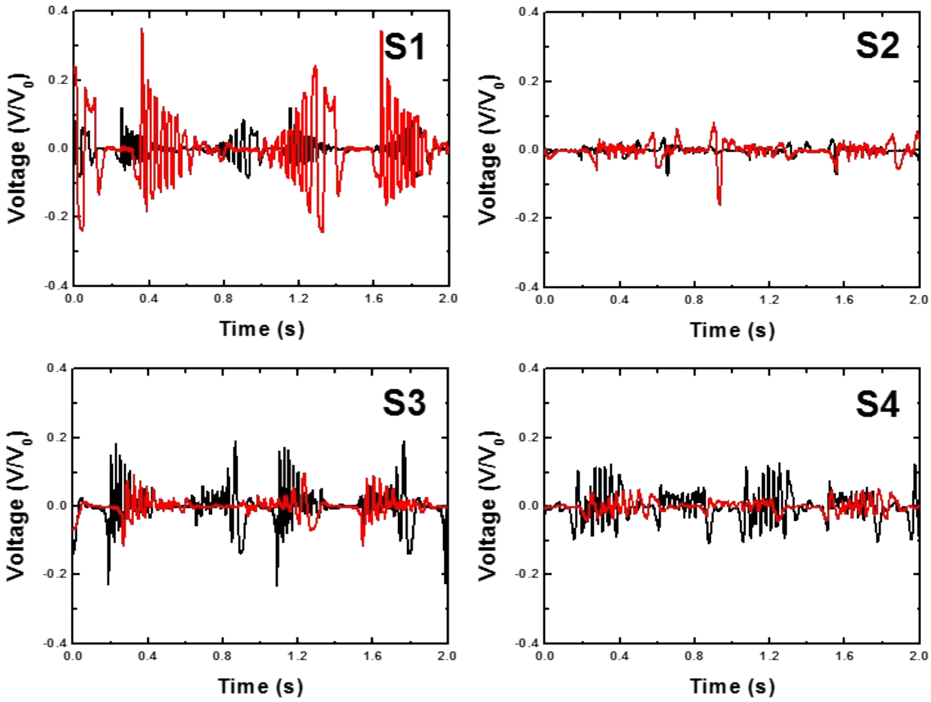

Figure S4-2. Nomalized signals. The red signals describes the nomalized tactile signals from the de-noise tactile signals (x(t), black).

S5. Feature extraction and selection for texture classification

The normalized tactile signal is converted to the power spectrum in frequency domain by taking the discrete-time Fourier transform (DTFT) as follows:

$$X(l) = \left| \sum_{m=0}^{L-1} \hat{x}(m) h(m) \exp\left(- \frac{j2\pi lm}{L} \right) \right|^2 \quad (9)$$

where l, $X(l)$, and $h(m)$ denote the frequency bin index, the magnitude at the l-th frequency bin, and window function, respectively. The power spectrum densities (PSDs) defined at the corresponding to the frequency bins are composing the feature vectors for the pattern recognition. The AUC method [2] is applied to determine the most distinguishable features to reduce the feature number for the training set. Each AUC is obtained by calculating the area under the receiver-operating-characteristics (ROC) curve which shows the trade-off characteristic between detection probability and the false-alarm probability. The decision rule for obtaining the AUC values is given by

$$d(x) = sgn\left[\exp\left(- \frac{\left| x - E(x^+) \right|^2}{2\sigma^2} \right) - \eta \right] \quad (10)$$

where $E(x^+)$ denotes the average of the feature vectors (i.e. PSDs) corresponding to the positive label and σ is the width of the kernel, and the signum function, $sgn(s)$, is defined as

$$sgn(s) = \begin{cases} -1, s < 0 \\ 0, s = 0 \\ 1, s > 0 \end{cases}. \quad (11)$$

where η denotes the threshold value for decision. The nonlinear decision rule is employed to fully consider nonlinear properties of the RBF kernel function [3]. This function is inspired from the nonlinear properties of the RBF kernel function for the SVM. Note that AUC of each sample is independently estimated, and then final AUC is averaged for finding the critical frequency bins for all samples. Since the adjacent frequency bins are substantially correlated, the triangle function is used to select the features by comparing discrimination capability. Instead using conventional machine learning-based texture classification methods, which use all the PSDs of frequency bins as features [4-8] or reduce the dimension of the feature vector through PCA [7-9], we select the superior discriminant features through the nonlinear AUC to achieve not only high classification accuracy, but also reduction of computational complexity.

S6. Texture classification based on the support vector machine (SVM)

The SVM is known as a supervised learning technique and has shown impressive performance in a variety of tasks for which the SVM classifier builds optimal hyper-planes that maximize the margin between classes [10]. In this work, we adopt the SVM classifier with a kernel trick which maps the input feature into a higher dimensional space to be used as a nonlinear classifier, as given by

$$d(x) = sgn\left(w^T \Phi(x) + b\right) \tag{13}$$

$$= sgn\left(\left(\sum_{X_k \in Y} a_k t_k \Phi(x_k)\right)^T \Phi(x) + b\right) \tag{14}$$

$$= sgn\left(\sum_{X_k \in Y} a_k t_k \Phi(x_k) \cdot \Phi(x) + b\right) \tag{15}$$

$$= sgn\left(\sum_{X_k \in Y} a_k t_k K(x_k, x) + b\right) \tag{16}$$

where T denotes the transpose of a vector or a matrix and Φ denotes the kernel function. Since the performance of each kernel function depends on the application, we primarily consider the RBF due to its wide applicability as shown by $K(x_k, x) = exp(-||x_k - x||^2/2\sigma^2)$. Note that, t_k is the class label with a positive label (+1) or negative label (-1), and a_k denotes the Lagrange multiplier coefficients. Originally, the SVM is a binary classifier, which maps the input feature vector into only two classes, positive or negative. However, there has been recent progress to extend the binary SVM into a multi-class problem like this multi-texture classification, including one-versus-one multi-class SVM [11], one-versus-rest multi-class SVM [12], decision tree-based multi-class SVM [13], and DAG multi-class SVM [14]. In this study, we use the one-versus-rest multi-class SVM as the classifier for texture classification since it is known to have the highest performance in terms of classification accuracy and computational efficiency.

S7. The classification accuracies with various scanning speeds.

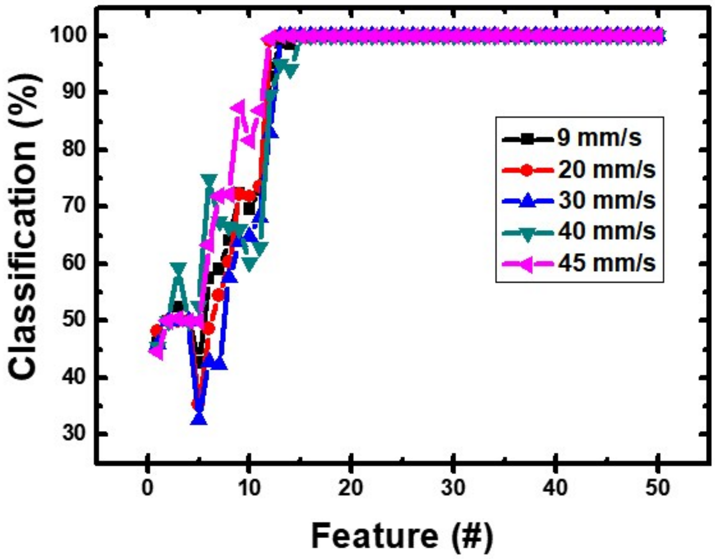

Figure S7. Classification accuracies of the 4 different tactile pattern samples various scanning speeds. The speeds are 9, 20, 30, 40, 45 mm/s, respectively.

S8. The process of feature extraction from the 12 complex fabrics.

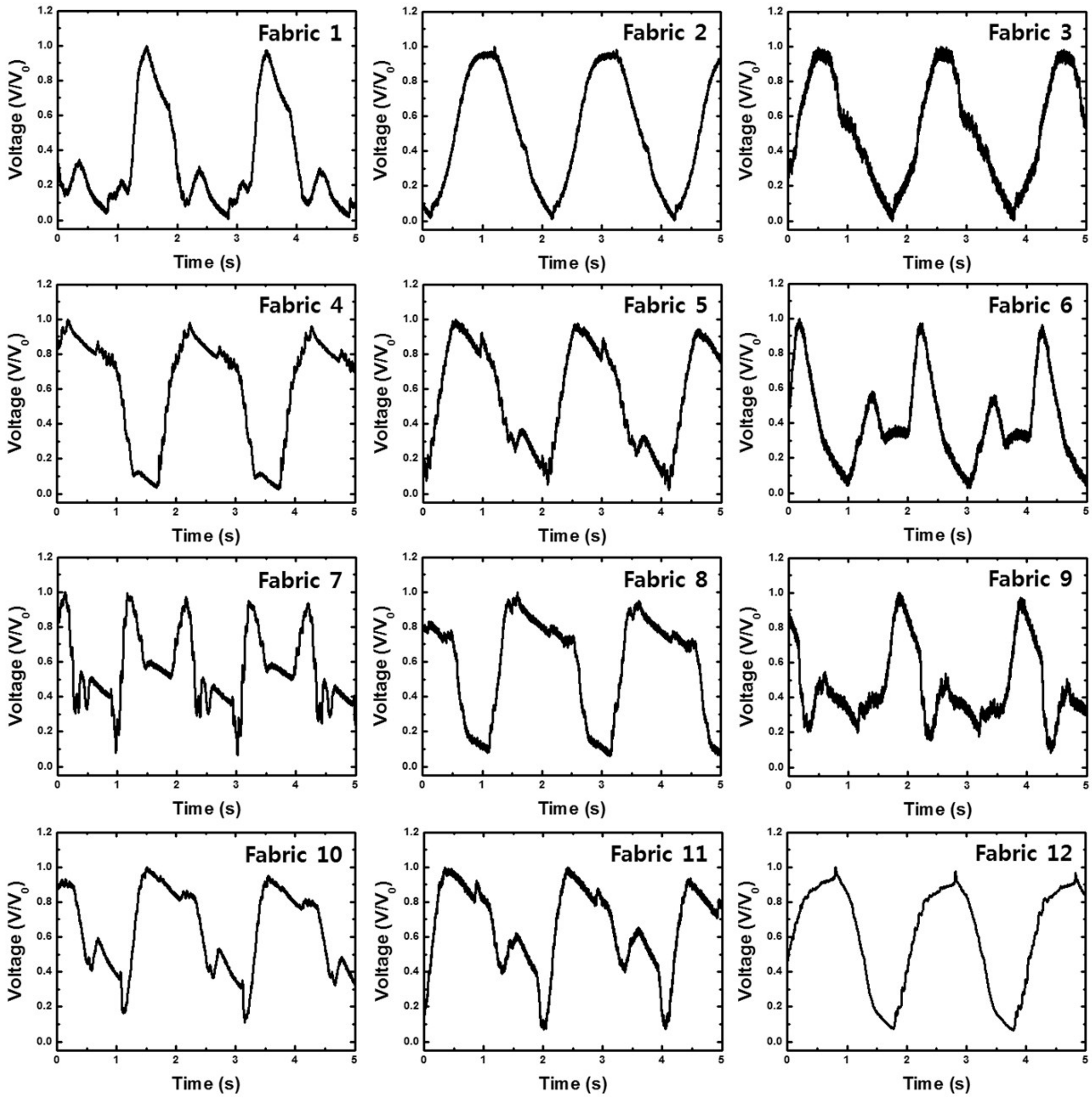

Figure S8-1. Sensor signals for the testing 12 fabrics. Each signal is obtained by consecutive scanning of forward direction and backward direction with rubbing of the sensor on the sample surface and sampling process ADC with sampling frequency of 1 kHz.

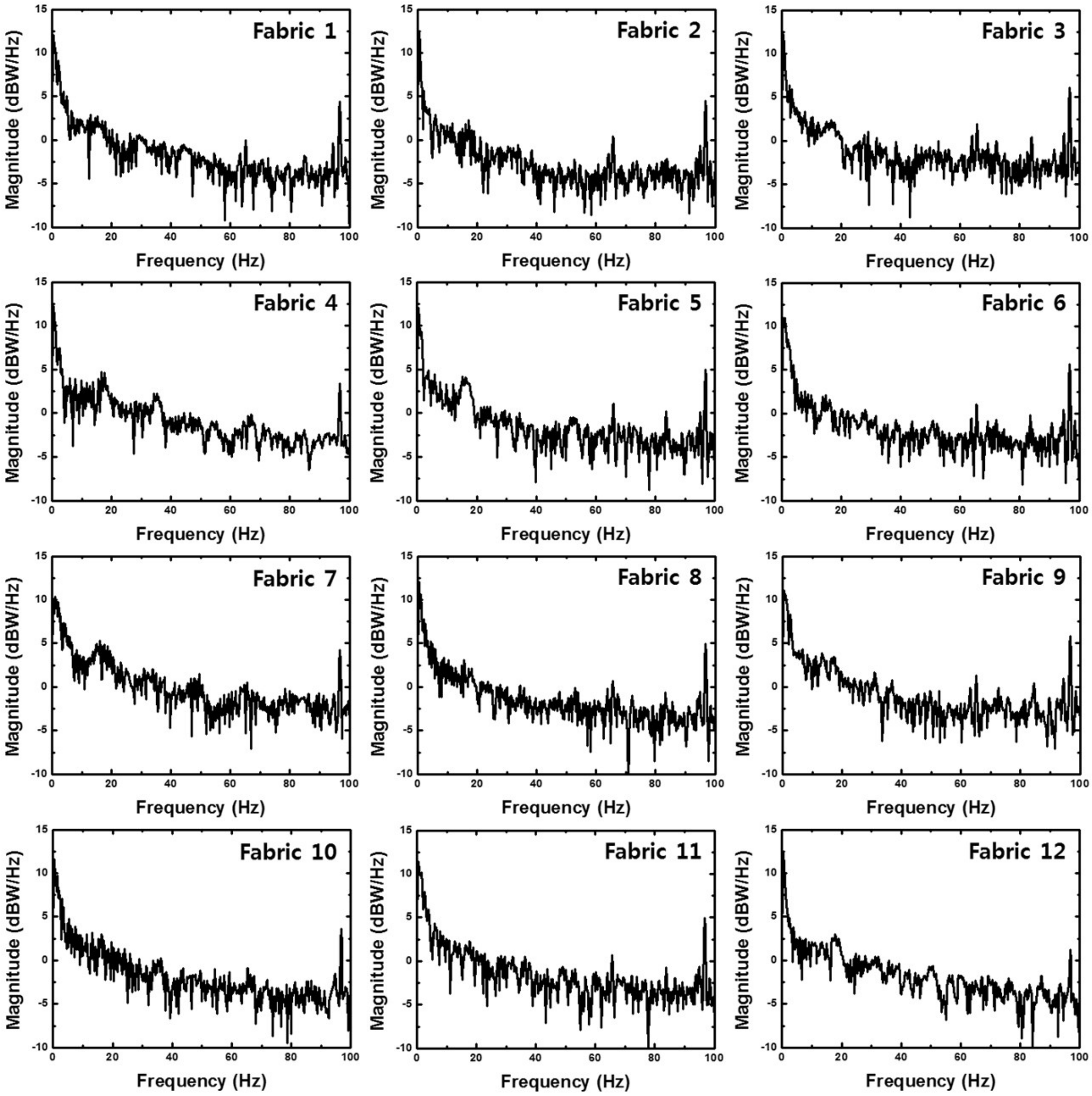

Figure S8-2. Power spectrum for the testing 12 fabrics. The tactile signals are obtained after the pre- and normalization processes to remove the noise and bias signal from the direct output of the sensor.

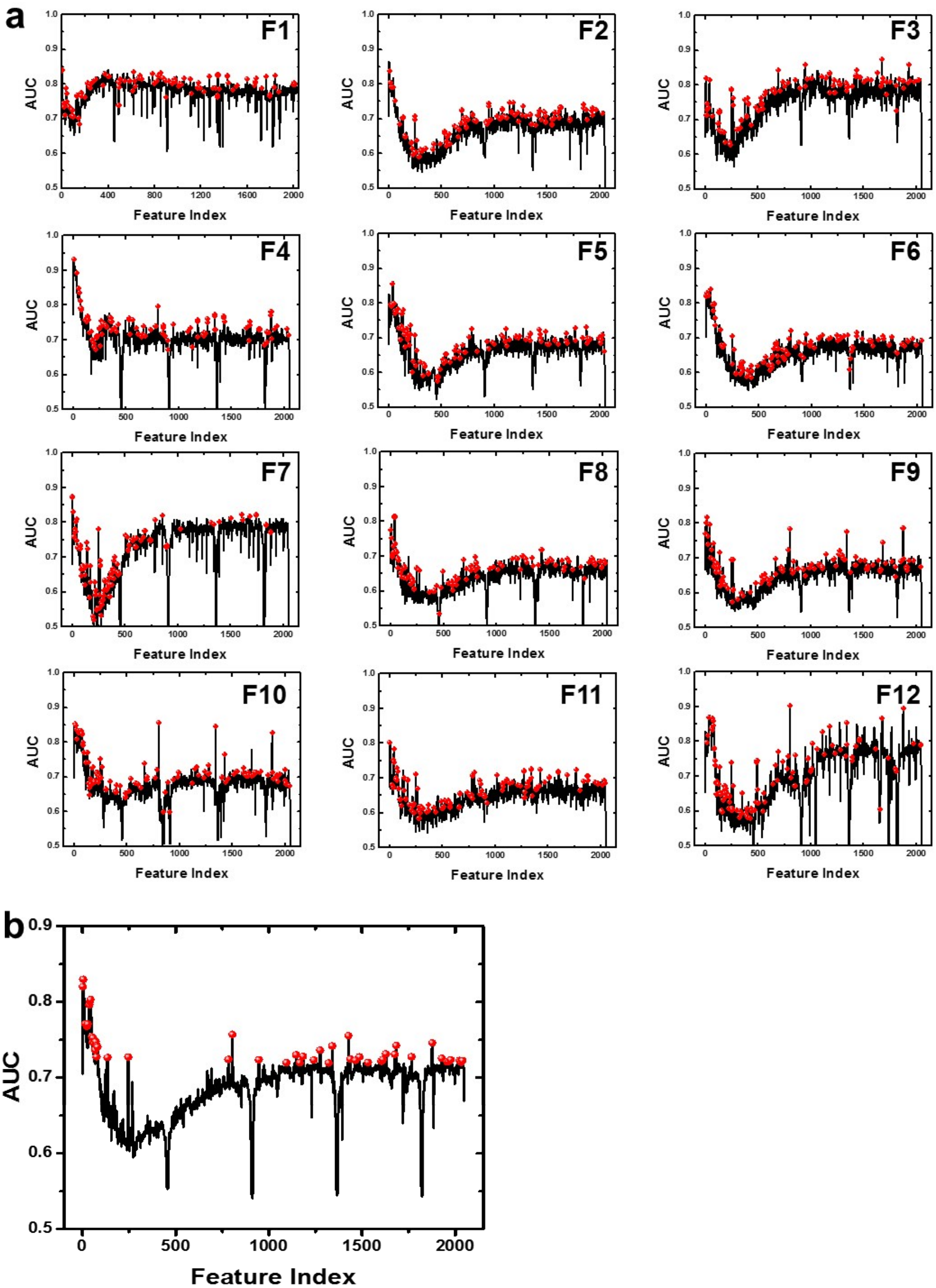

Figure S8-3. AUCs for the testing 12 fabrics. a) AUC distributions of each feature (line) obtained from fabrics. The circle marks represent local maxima indicating the frequency bins addressing the most distidushable features. b) Averaged AUCs for 12 samples where the circle marks represent top 50 AUCs.

S9. Tactile patterns for 3 fabrics prepared for prediction

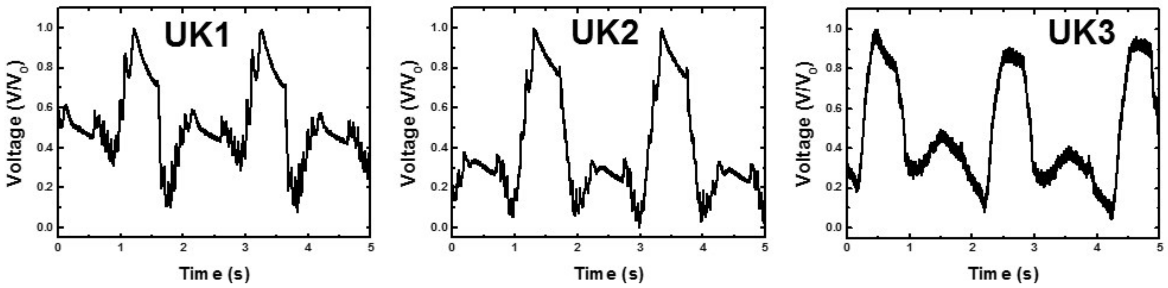

Figure S9-1. Sensor signals for the unknown 3 fabrics. Each signal is obtained by consecutive scanning of forward direction and backward direction with rubbing of the sensor on the sample surface and sampling process ADC with sampling frequency of 1 kHz.

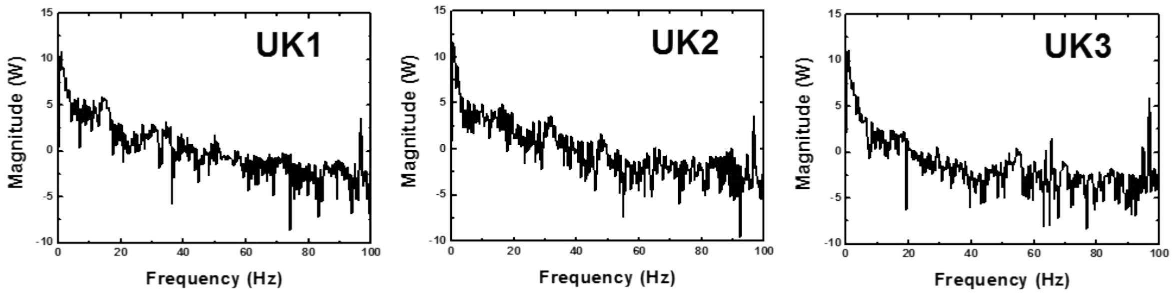

Figure S9-2. Power spectrum for the unknown 3 fabrics. The tactile signals are obtained after the pre- and normalization processes to remove the noise and bias signal from the direct output of the sensor.

References

1. Y. Ephraim. D. Malah, *IEEE Trans. on Acoust., Speech, and Signal Process.*, 1984, **32**, 1109-1121.
2. R. Wang, K. Tang, *IEEE Proc. International Conference on Data Mining Workshop,* 2009, 400-405.
3. D. Enqing, L. Guizhong, Z. Yatong, Z. Xiaodi, *IEEE Proc. International Conference on Signal Processing,* 2002, 1124-1127.
4. Y. Tanaka, Y. Horita, A. Sano, H. Fujimoto, *IEEE Proc. World Haptics Conference,* 2011, 621-626.
5. D. S. Chathuranga, S. Hirai, *IEEE Proc. International Conference on Advanced Intelligent Mechatronics,* 2013, 1667-1674.
6. A. Song, Y. Han, H. Hu, J. Li *IEEE Trans. on Inst. and Meas.,* 2014, **63**, 1739-1747.
7. H. Hu, Y. Han, A. Song, S. Chen, C. Wang, Z. Wang, *Sensors,* 2014, **14**, 4899-4913.
8. A. G. Equiluz, I. Rano, S. A. Coleman, T. M. Ginnity, *IEEE/RSJ International Conference on Intelligent Robots and System,* 2016, 4912-4917.
9. Y. Tanaka, Y. Horita, A. Sano, *Proc. Eurohaptics,* 2014, 169-174.
10. V. Vapnik, *The Nature of Statistical Learning Theory*, (Springer-Verlag, New York, 1995).
11. U. Krebel, *Pairwise classification and support vector machines*, (MIT Press, Cambridge, 1999).
12. V. Vapnik, *Statistical Learning Theory*, (Wiley, New York, 1998).
13. F. Takahashi, S. Abe, *Proc. Advances in Neural Information Processing Systems,* 2014, **3**, 1418-1422.
14. J. Platt, N. Cristianini, J. Shawe-taylor, *Large margin DAGs for multiclass classification*, (MIT Press, Cambridge, 2000).